Eur. Phys. J. B **39**, 433–440 (2004)
DOI: 10.1140/epjb/e2004-00214-x

THE EUROPEAN PHYSICAL JOURNAL B

Spectroscopic and dc-transport investigations of the electronic properties of $TaSe_3$

A. Perucchi[1], C. Søndergaard[2], S. Mitrovic[2], M. Grioni[2], N. Barisic[3], H. Berger[3], L. Forró[3], and L. Degiorgi[4,1,a]

[1] Laboratorium für Festkörperphysik, ETH Zürich, 8093 Zürich, Switzerland
[2] Institut de Physique des Nanostructures, EPF Lausanne, 1015 Lausanne, Switzerland
[3] Institut de Physique de La Matière Complexe, EPF Lausanne, 1015 Lausanne, Switzerland
[4] Paul Scherrer Institute, 5232 Villigen

Received 16 February 2004 / Received in final form 27 April 2004
Published online 23 July 2004 –

Abstract. $TaSe_3$ belongs to a class of low-dimensional materials characterized by the interplay and competition between dimensionality crossover and broken symmetry ground states. A comprehensive study by dc-transport, optical, and angle-resolved photoemission (ARPES) experiments shows that the electronic properties of this compound are strongly anisotropic between the chain and the transverse crystallographic direction. Even though $TaSe_3$ fails to undergo a charge-density-wave (CDW) phase transition, we found evidence for short range order CDW segments, which progressively disappear with decreasing temperature.

PACS. 78.20.-e Optical properties of bulk materials and thin films – 71.30.+h Metal-insulator transitions and other electronic transitions – 71.45.Lr Charge-density-wave systems

1 Introduction

Restricted dimensionality has become an important subject of research in solid state physics [1]. First of all, a general characteristic of low-dimensional solids – i.e., materials which can be considered as an ensemble of weakly coupled linear chains or layered-like entities – is the instability towards the formation of charge- or spin-density-wave (CDW and SDW) states [2]. These are typical broken-symmetry ground states driven by the electron-phonon or electron-electron interaction for CDW or SDW, respectively. The density wave phase transitions also imply a gapping of the Fermi surface, as a consequence of the $q = 2k_F$ (k_F being the Fermi wave vector) nesting [2]. Considerable interest has also been raised by the peculiar normal state properties of correlated electron systems in low dimensions, which deviate considerably from the standard Fermi liquid scenario [3]. Specifically, in one dimension the low-energy excitations of the Luttinger liquid state predicted by theory exhibit non-Fermi-liquid properties like spin-charge separation.

The role of the low-dimensionality is probably essential in a variety of *real* materials, including the inorganic and organic linear chain compounds as well as the layered-like high temperature superconductors [1,2]. In several low-dimensional materials peculiar charge transport and dynamics have been established. For instance, metallic-like transport was found for very high values of the resistivity [4], with mean free paths of the order of the lattice constant. The term "bad metal" was coined in order to point out the inadequacy of ideas based on the concept of well defined quasiparticles and extended electronic states [4,5]. In some cases, the peculiar power-law behaviours in the spectroscopic (optical and angle-resolved photoelectron (ARPES)) properties and unusual features in the charge dynamics could be qualitatively reconciled with the Tomonaga-Luttinger or Luther-Emery scenarios [3].

The transition metal trichalcogenides XSe_3 (X = Ta and Nb) are among the most interesting materials displaying a competition and/or interplay between dimensionality crossover and broken symmetry ground states. While they both remain metallic with decreasing temperature, the dimensionality of the electronic structure is tuned by the effective coupling between the chains. The Nb-compound exhibits properties typical for a pseudogapped quasi one-dimensional system, while the Ta-compound resembles more closely an anisotropic conductor. The more pronounced low-dimensionality of the former corresponds to a much less warped Fermi surface (FS), which favors $2k_F$ nesting and partial gapping of the FS. Indeed, $NbSe_3$ undergoes two CDW phase transitions at $T_1 = 145$ and $T_2 = 59$ K (Ref. [6]). Recently, investigations of the electrodynamic response (Ref. [7]) and of the ARPES spectral function [8] of $NbSe_3$ give evidence for pseudogap

[a] e-mail: degiorgi@solid.phys.ethz.ch

features associated to the CDW phase transitions. The optical and ARPES responses are also strongly dominated by precursor effects, which hint to the relevant role played by 1D fluctuations [7,8]. In $TaSe_3$, on the other hand, no CDW transition has been identified so far [9].

These differences demand a more detailed study of $TaSe_3$. The availability of high quality single crystal of sufficiently large size allowed us to measure the dc electrical transport and the reflectivity both along and perpendicular to the 1D chains and to perform the first ARPES measurements on this material. We will first introduce the dc-transport properties and then the spectroscopic results. We will then discuss the notable aspects of the electronic structure of $TaSe_3$ and draw a comparison with $NbSe_3$ and also with related families of low dimensional systems, like the quasi-two-dimensional dichalcogenides $2H-XSe_2$, and the prototypical CDW or SDW materials.

2 Experiment and results

High purity single crystals of $TaSe_3$ were grown by direct sublimation of elemental Ta and Se with a slight excess of Se in an evacuated quartz ampoule between 660 and 700 °C for a period of ten weeks [10]. Like other "quasi-1D" systems, $TaSe_3$ is a layered material with strongly anisotropic properties. The fundamental structural units are parallel trigonal-prismatic $TaSe_3$ chains which run along the **b** axis of the monoclinic structure ($a = 10.4$ Å; $b = 3.5$ Å; $c = 9.8$ Å; $\beta = 106°$), forming infinite (**b**, **a**+**c**) layers. "Equilateral-" (E) and "isosceles" (I) chains alternate within each layer. In the former, the base of each $TaSe_3$ prism is an equilateral triangle, with 3 equivalent Se^{2-} ions. In the latter the triangles are isosceles, with one short Se-Se distance so that, from a chemical point of view, they can be described as $(Se^{2-} + Se_2^{2-})$. In the ionic limit, Ta has an average $Ta^{5+}(d^0)$ configuration, and $TaSe_3$ should be an insulator. In reality, it is a semimetal, due to the hybridization of Ta 5*d* and Se 4*p* states, and to a possible indirect overlap of the valence and conduction bands. A strong interaction along each chain is responsible for the marked 1D character, predicted by band structure calculations, and confirmed here experimentally.

The dc electrical resistivity was measured by the four point contact method. The temperature dependence along the chain *b*-axis and the transverse axis (i.e., along the $a + c$ direction, perpendicular to the *b*-axis) is shown in Figure 1. Along the *b*-axis ρ_b(T) decreases with decreasing temperature in a metallic-like fashion and confirms previous data [9]. Measurements up to 500 K show that the *b*-axis resistivity does not saturate at high temperatures, but has rather a linear temperature dependence (see inset of Fig. 1). Along the transverse axis $\rho_{transv.}(T)$ first increases with decreasing temperature displaying a broad maximum at 130 K and then decreases with a pronounced drop towards low temperatures. Such an anisotropic behaviour of $\rho(T)$ bears some similarities with findings in layered transition metal dichalcogenides [11] and in high temperature superconductors (HTC) (Refs. [1] and [12]). The overall behaviour of $\rho(T)$ along both the chain and transverse axes also looks very similar to the (normal state) transport properties of the organic Bechgaard salts [13].

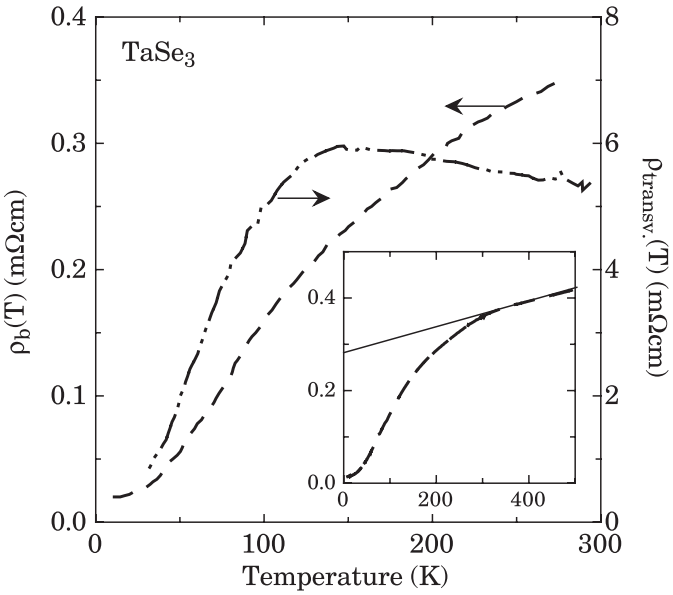

Fig. 1. Temperature dependence of the resistivity along the transverse and chain *b*-axis. The inset emphasizes the high-temperature linear behaviour of $\rho_b(T)$.

The optical reflectivity $R(\omega)$ was measured on samples with well aligned crystals, forming a surface of 2×2 mm^2, from the far-infrared (FIR) up to the ultra violet (UV) and between 2 and 300 K. Reflectivity curves were measured with light polarized either along the chain *b*-axis or the transverse axis. Details pertaining to the experiment can be obtained elsewhere [14]. Figure 2 shows $R(\omega)$ for two selected temperatures for each polarization. For the optical response we choose the same layout in the data presentation as for $NbSe_3$ (Ref. [7]), in order to facilitate the comparison. While $R(\omega)$ is metallic at any temperatures and for both polarization directions, there is a remarkable anisotropy between the two crystallographic directions. For the *b*-axis, we recognize a rather sharp plasma edge with onset at about 3000 cm^{-1}. For the transverse axis, the plasma edge is broader, signaling an overdamped-like behaviour of the charge carriers. The temperature dependence along the two axes is distinct: for the *b*-axis $R(\omega)$ progressively increases from FIR up to the plasma edge with decreasing temperature; for the transverse axis there is first the formation of a broad feature at 1000 cm^{-1}, followed by a depletion in FIR and then by a sharp upturn of $R(\omega)$ below about 100 cm^{-1}. The enhancement of $R(\omega)$ at low frequencies ($\omega < 150$ cm^{-1}) with decreasing temperature for both polarizations is in accordance with the overall metallic behaviour of ρ(T) at low temperatures (Fig. 1). For both polarizations there is also the appearance of phonon modes with decreasing temperature, which are rather sharp and particularly visible along the transverse axis. Above the plasma edge features, additional absorptions ascribed to the electronic interband transitions can be identified [15].

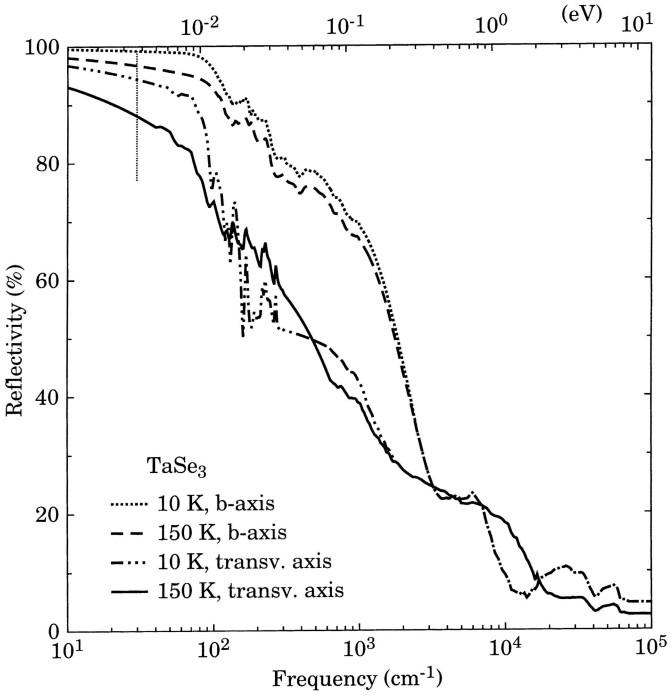

Fig. 2. Optical reflectivity $R(\omega)$ in $TaSe_3$ along both polarization directions and at two selected temperatures (10 and 150 K). The thin dotted line marks the frequency below which the Hagen-Rubens extrapolation has been performed.

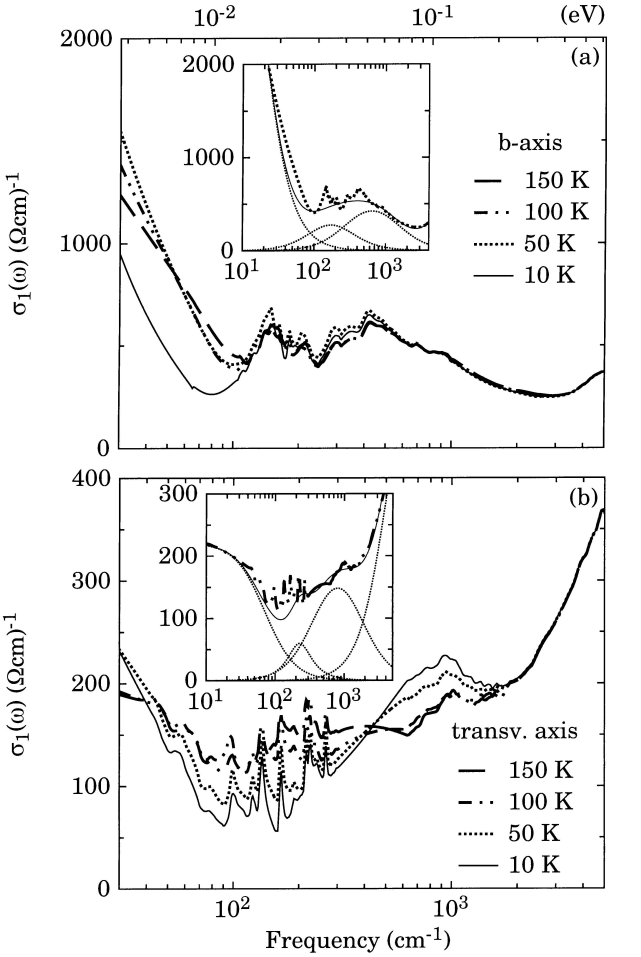

Fig. 3. Real part $\sigma_1(\omega)$ of the optical conductivity above 30 cm^{-1} as a function of temperature along (a) the chain b-axis and (b) the transverse axis. The insets show the data at 50 (b-axis) and 100 K (transverse axis) with the total fit and its components (the sharp phonon modes are omitted for clarity, see text).

Kramers-Kronig (KK) transformations [14] allow us to calculate the real part $\sigma_1(\omega)$ of the optical conductivity. To this end, standard high frequency extrapolations $R(\omega) \sim \omega^{-s}$ (with $2 < s < 4$) were employed in order to extend the data set above 10^5 cm^{-1} into the electronic continuum. At low frequencies, $R(\omega)$ was extrapolated with the Hagen-Rubens (HR) law $R(\omega) = 1 - 2\sqrt{\omega/\sigma_{dc}}$ with conductivity values (σ_{dc}) in agreement with the dc transport data (Fig. 1). Figure 3 details the temperature dependence of $\sigma_1(\omega)$ for both polarizations and for frequencies below 5000 cm^{-1}. At low frequencies ($\omega < 150$ cm^{-1}) there is a narrowing of $\sigma_1(\omega)$ for both polarizations with decreasing temperature. Similarly to $NbSe_3$ (Ref. [7]), this narrowing of $\sigma_1(\omega)$ at low frequencies and temperatures follows from the steep increase of $R(\omega)$ below about 200 cm^{-1} along the c-axis and the overall enhanced $R(\omega)$ spectrum along the b-axis (Fig. 2). At low temperatures the narrowing is so strong that the spectral weight of the effective (Drude) metallic component falls almost entirely below our data's low frequency limit ($\sim$30 cm^{-1}). This leads to an apparent disagreement in Figure 3 between $\sigma_1(\omega \to 0)$ and σ_{dc} (Fig. 1). We caution that the low frequency behaviour of $\sigma_1(\omega)$ obviously results from the HR extrapolation used for $R(\omega)$ below 30 cm^{-1}. At high frequencies, we observe a broad mid-infrared feature along the b-axis with overlapped absorptions due to the phonon modes but at variance with $NbSe_3$ (Ref. [7]) no remarkable suppression of spectral weight in the infrared range with decreasing temperature. Along the transverse axis, on the other hand, the temperature dependence of $\sigma_1(\omega)$ in $TaSe_3$ is similar to that of $NbSe_3$ (Ref. [7]). There is a clear suppression of spectral weight in the range between 100 and 500 cm^{-1}, which shifts at high frequencies and piles up at the absorption at about 1000 cm^{-1}. This happens most remarkably below 100 K and is very much reminiscent of a (pseudo)-gap opening. Furthermore, several sharp phonon lines clearly appear in $\sigma_1(\omega)$ with decreasing temperature along the transverse axis.

Photoemission measurements were performed at Lausanne and at the Wisconsin Synchrotron Radiation Center (SRC), with total experimental energy resolution $\Delta E =$ 15 meV, and momentum resolution $\Delta k = 0.015$ $Å^{-1}$. The single crystal samples were cleaved in ultra high vacuum (10^{-10} mbar range) to expose clean ($a + c$) planes containing the $Ta - Se$ chains. Scanning tunneling microscopy (STM) measurements [16] have shown that cleavage produces atomically ordered surfaces. The Fermi level position was determined with an accuracy of ± 1 meV by measuring the metallic cutoff of a polycrystalline Au film.

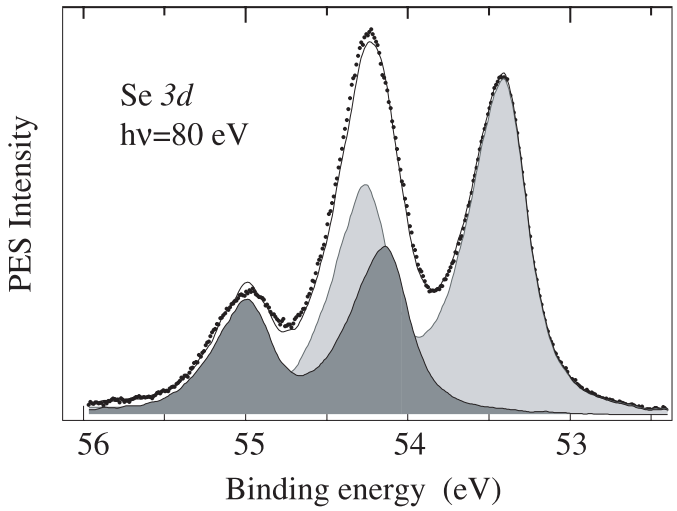

Fig. 4. Se 3d core levels ($h\nu$ = 80 eV) after subtraction of a Shirley background. The complex line shape is reproduced by the sum of two ($j = 5/2; 3/2$) doublets, with identical line shapes, 2:1 relative intensities, and shifted by 0.73 eV. They correspond to the inequivalent Se sites in the $TaSe_3$ structure.

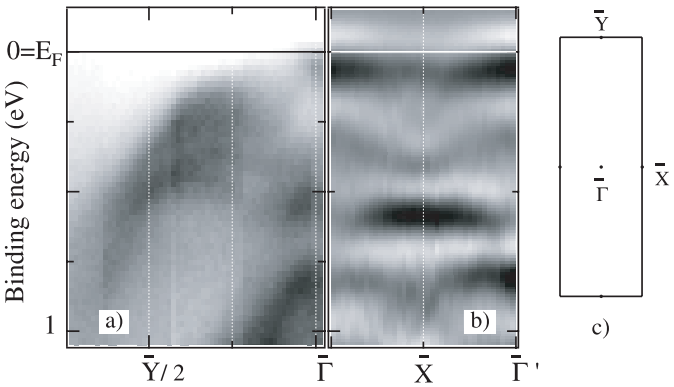

Fig. 5. Grey-scale ARPES intensity maps (white is lowest, black is largest intensity) a) Along the b ($\bar{\Gamma}\bar{Y}$) chain direction ($h\nu = 25$ eV; $T = 100$ K). The main dispersing feature with a maximum at $k \sim 0.3$ $\bar{\Gamma}\bar{Y}$ is a hybrid Ta 5d–Se 4p band predicted by band structure calculations. Further band features are seen near Γ at ∼0.1, 0.5 and 0.8 eV; b) Along the ΓX direction perpendicular to the chains. In order to enhance the weaker band signatures the second derivative of the ARPES signal is shown. c) Scheme of the surface Brillouin zone.

The Se 3d core level spectrum (Fig. 4) indicates the presence of inequivalent sites. It exhibits 3 distinct peaks instead of the expected spin-orbit split ($j = 3/2; 5/2$) doublet. After subtraction of a standard Shirley background, we decomposed it into the sum of a main spin-orbit doublet and a shifted and attenuated replica. Rather than using a standard analytical expression with free parameters (width, asymmetry) [17] we self-consistently determined the lineshape from the data. The common lineshape of each spin-orbit component was forced to fit the leading and trailing edges of the experimental spectrum, where the overlap with other components is small. The spin-orbit doublet was then constructed using the statistical branching ratio $BR = 2/3$ and an energy separation Δ_{SO} compatible with tabulated values (0.8−0.9 eV) of the Se 3d spin-orbit splitting. The fit was performed by varying Δ_{SO}, BR as well as the energy shift ΔE and intensity ratio R of the main doublet and replica. An excellent fit is obtained for the following set of parameters: $BR = 0.65$, $\Delta_{\rm SO} = 0.85$ eV, $\Delta E = 0.73$ eV and $R = 0.5$. The latter value supports the proposed bonding configuration for the Se ions: $3(\mathrm{Se})^{2-}$ in the E chain and $(\mathrm{Se})^{2-} + (\mathrm{Se}_2)^{2-}$ in the I chains, with an overall 2:1 ratio between the two different sites. Notice also that the signal from the "minority" $(\mathrm{Se}_2)^{2-}$ sites correctly appears at higher binding energy, as a consequence of the smaller local electron density. Similarly, the Ta 4f core level spectrum (not shown) does not exhibit a simple (Lorentzian, Voigt or Doniach-Sunjic) [17] lineshape, suggesting the possibility of inequivalent, albeit not resolved, Ta sites.

Figure 5 summarizes the ARPES results for the directions parallel to the chains ($\bar{\Gamma}\bar{Y}$), and perpendicular, along the ($\bar{\Gamma}\bar{X}$) direction of the surface Brillouin zone (BZ). In the grey-scale images white corresponds to the lowest, and black to the largest ARPES intensity. The prominent maximum at ∼0.3 ($\bar{\Gamma}\bar{Y}$) is due to the overlap of Ta d_{z^2} and Se 4p bands dispersing upwards from their minima at $\bar{\Gamma}$ (at ∼0.5 eV) and $\bar{Y}$, respectively [15]. In the calculation [15] the Fermi level cuts this band, yielding a hole pocket. The intensity plot and a careful analysis of the individual spectra around the maximum at 0.3 $\bar{\Gamma}\bar{X}$ (not shown) do not confirm the existence of a hole Fermi surface. We cannot however totally exclude that the band maximum actually crosses E_F elsewhere in the Brillouin zone. A full band mapping, including the direction perpendicular to the layers, would be necessary to clarify this point. Moreover, the possibility that the bands are modified near E_F by an underlying CDW instability must be taken into account (see below). Additional features are visible near $\bar{\Gamma}$ at ∼1 eV and close to E_F.

The dispersion along the perpendicular ($\bar{\Gamma}\bar{X}\bar{\Gamma}$) direction is small (<0.15 eV) for all features, providing a microscopic justification for the definition of $TaSe_3$ as a 1D compound. The second derivative of the ARPES intensity map is shown in the figure, in order to enhance the visibility of the weaker features. The experimental band structure – periodicity and intensity – reflects the symmetry of the $(a+c)$ layer, and attests to the good crystalline order of the cleaved surface.

The calculated bands for the 3D structure [15] exhibit a small electron pocket near Γ, where the Fermi level intersects the bottom of a distinct Ta d_{z^2} band. However, the robustness of this prediction is not clear, since the pocket is not present for an isolated $(a + c)$ layer, and it is also affected by dispersion perpendicular to the chains [18]. Careful measurements within a narrow portion of the BZ near Γ (Fig. 6), do not show the expected pocket, but rather a fast dispersing band with a maximum at Γ, very close to the Fermi level ($E_B = 60$ meV). The overall shape of the band is well described by a parabola with a maximum slightly above E_F, but the dispersion is suddenly truncated just before the actual crossing, as indicated by

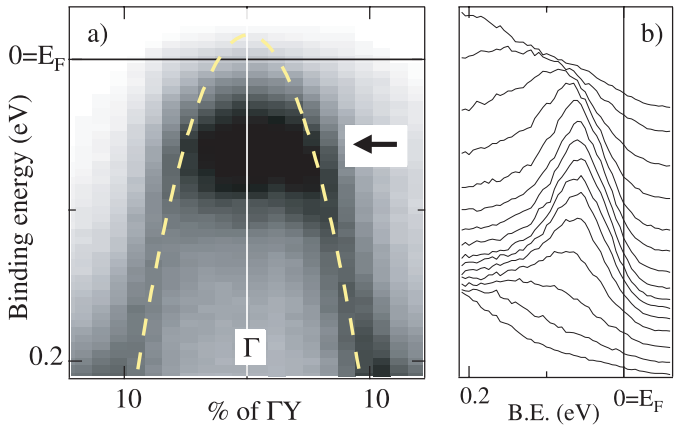

Fig. 6. a) ARPES intensity map showing a close-up of the valence band ($h\nu = 25$ eV). The band is well described by a parabola (dashed line), except for a flat region (arrow) around $\bar{\Gamma}$. b) ARPES spectra extracted from the center of the map of a), showing the flat band region.

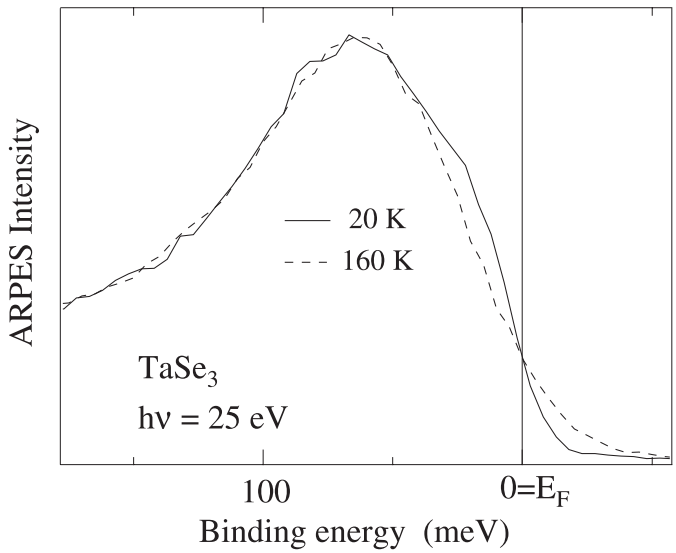

Fig. 7. ARPES spectra measured at two temperatures (160 and 20 K) from the flat region at the top of the band of Figure 6. The line shape of the $T = 160$ K spectrum is compatible with that of the $T = 20$ K spectrum after thermal broadening.

the arrow. The striking narrow ($\Delta k \sim 0.1$ Å) flat region is confirmed by the series of spectra (Fig. 6b) extracted from the central part of the map. A parabolic band with a maximum at Γ is predicted well below (0.35 eV) E_F for an isolated $(a+c)$ layer, but the maximum apparently moves above E_F for a smaller structural unit consisting of two coupled chains [15]. The experimental ARPES result is closer to the latter situation, suggesting that the tight-binding calculation may overestimate in-plane interactions.

The spectra of Figure 7, measured at 20 and 160 K, are representative of the ARPES data for the whole flat region around Γ. The 20 K spectrum exhibits both a broad peak at $E = 60$ meV, and a clear Fermi edge, whose width is determined by the experimental resolution and temperature. It is interesting to notice that at both temperatures the spectral weight at E_F is clearly nonzero. At 160 K the peak position remains constant; the leading edge is broader but, within the experimental accuracy in the Fermi level position, the 160 and 20 K spectra are identical, including the intensity at E_F, if thermal broadening is explicitly taken into account.

3 Discussion

The linear T-dependence of the b-axis resistivity above 300 K indicates a strong elastic scattering mechanism which cannot originate from static defects or impurities in such a highly crystalline structure. Furthermore this scattering mechanism gradually freezes out below 300 K. A similar effect has been observed in 2H−$TaSe_2$: short coherence length CDW segments diffuse the conduction electrons above the long range ordering temperature of 120 K, while the resistivity strongly decreases below this temperature due to the reduced scattering rate. A further analogy can be drawn with the underdoped cuprates, where the increased mobility of the charge carriers below a characteristic temperature $T^*(T^* > T_c)$ is believed to arise from the freezing out of magnetic excitations. Structural studies in $TaSe_3$ have not yet detected a CDW formation, although its proximity to trichalcogenide and dichalcogenide CDW compounds makes it likely. We remark at this point that the formation of short range order CDW segments was identified in prototype 1D CDW systems above the critical phase transition temperature as a consequence of the precursor effects [19]. These entities determine the transport and spectroscopic properties of several CDW materials, like the "blue bronze" $K_{0.3}MoO_3$ and $NbSe_3$ (Refs. [7] and [19]), in the fluctuation regime. At high temperatures these CDW segments can be also viewed as local modes or molecular states (MS) [9]. A CDW phase transition would then be possible if the CDW segments or MS's developed long range order. Failure to develop a CDW condensate could come from the disappearance of such local modes at low temperatures, since the atomic displacements needed to stabilize them become thermally inaccessible [20]. Therefore, $TaSe_3$ is at the verge of a transition into a CDW state [9]. Interestingly enough a CDW condensate can be stabilized in $TaSe_3$ under uniaxial strain [21].

The c-axis resistivity has a broad maximum around $T_0 = 130$ K below which it shows a metallic-like temperature behavior, although its value is beyond the Ioffe-Regel limit for coherent electronic transport. There is no detailed theoretical description for $d\rho/dT > 0$ for carriers with mean-free path shorter than the lattice spacing, although it is very common in anisotropic conductors. An empirical description for metallic and non-metallic dc-transport considers resonant tunneling and phonon assisted hopping for the two regimes, respectively. In our case it would mean, that a source of disorder, which imposes temperature activated transport, is switched off gradually, enabling coherent tunneling of the carriers below 130 K. Similar dc

transport results on layered metallic systems [22] were recently interpreted as an indication for a dimensionality crossover correlated with the presence of coherent quasiparticles within the layers.

In order to catch the overall temperature dependence of $\sigma(\omega) = \sigma_1(\omega) + i\sigma_2(\omega)$ and to identify the relevant excitations, we have applied the Lorentz-Drude (LD) phenomenological approach, already used for $NbSe_3$ (Refs. [7] and [14]):

$$\sigma(\omega) = \frac{\omega_{pD}^2}{4\pi}\frac{\tau}{1 - i\omega\tau} + \sum_j \frac{\omega_{pj}^2}{4\pi}\frac{\omega}{i(\omega_j^2 - \omega^2) + \gamma_j\omega} \qquad (1)$$

where ω_j, γ_j and ω_{pj} are the resonance frequency, the damping and the mode strength of the Lorentz harmonic oscillator (h.o.). The Drude contribution (first term in Eq. (1)) of the itinerant charge carriers is obtained by setting $\omega_j = 0$ and the corresponding oscillator strength is the squared plasma frequency $\omega_{pD}^2 = 4\pi ne^2/m^*$ (n is the density and m^* is the effective mass of the itinerant particles) and $\Gamma_D = 1/\tau$ is the free charge carriers scattering rate. The LD model also sheds light on the spectral weight redistribution as a function of temperature among the various excitations. Besides the Drude component, two Lorentz h.o.'s are necessary for describing the far- and mid-infrared spectral range of $\sigma_1(\omega)$. These components, which also turn out to fully incorporate the temperature dependence of $\sigma_1(\omega)$ (see below), are shown for two selected temperatures in the insets of Figure 3. The high frequency excitations, due to the electronic interband transitions, and the sharp absorptions in FIR, due to the phonon modes, are also accounted for by Lorentz h.o.'s. The former turn out to be temperature independent, while the phonons are weakly temperature dependent and marginally contribute to the total spectral weight.

Along the b-axis there is a shift of spectral weight from the high frequency tail of the absorption, represented by the h.o. at 645 cm^{-1} (∼0.08 eV), towards low frequencies. The lost spectral weight with decreasing temperature is relocated into the h.o. at 174 cm^{-1} (∼0.02 eV) and the Drude term. Along the transverse axis, we encounter a different temperature dependence, consisting in the transfer of spectral weight from the first h.o. at 226 cm^{-1} (∼0.03 eV) to the h.o. at 803 cm^{-1} (∼0.1 eV). This mimics the opening of a pseudogap excitation. The Drude term along the transverse axis has a constant spectral weight as a function of temperature. The redistribution of spectral weight is such that the total weight is conserved at any temperature and fully recovered up to 5000 cm^{-1} for both polarizations [7]. In this regard, the XSe_3 series, like the $2H{-}XSe_2$ dichalcogenides [5], do not show any sum rule violation as it is the case for the HTC systems [23]. The temperature dependence of the spectral weight redistribution among the Drude term and the low frequency h.o.'s is shown in Figures 8a and b for both polarization directions. Interestingly enough, the most relevant changes in spectral weight occur around 100 K, therefore very close to T_0 (Fig. 1).

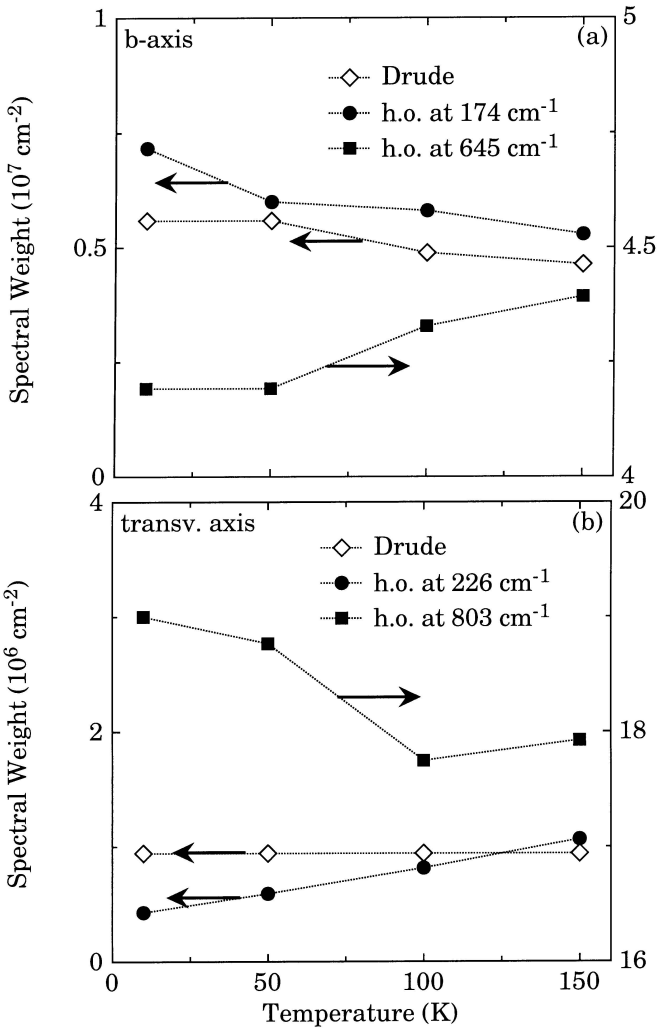

Fig. 8. Temperature dependence of the spectral weight of the Drude term and of the infrared Lorentz harmonic oscillators (a) along the chain b-axis and (b) along the transverse axis. The left and right y-axis scales are different but the relative spectral weight difference is the same on both axes.

The opening of a pseudogap at about 800 cm^{-1} along the transverse axis in the Ta-compound looks very similar to the finding in $NbSe_3$ (Ref. [7]). Nevertheless, while the spectral weight in $NbSe_3$ was shifted from the Drude component to the high frequency absorption, in $TaSe_3$ the shift of spectral weight is among the low (226 cm^{-1}) and high (803 cm^{-1}) frequency excitation (Fig. 8b). Consequently, the (pseudo)-gap in $TaSe_3$ cannot be due to the suppression of portions of the FS, and we propose a band structure effect as the possible origin. The absence of FS gapping is also confirmed by the b-axis data. In contrast to $NbSe_3$, there is again no indication for a depletion of FS in $TaSe_3$ along the chain b-axis. In fact, the Drude component and its high-frequency tail (h.o. at 174 cm^{-1}) gain the spectral weight (Fig. 8a), which is lost by the absorption at about 645 cm^{-1}. We propose a scenario where the molecular states progressively overlap with decreasing

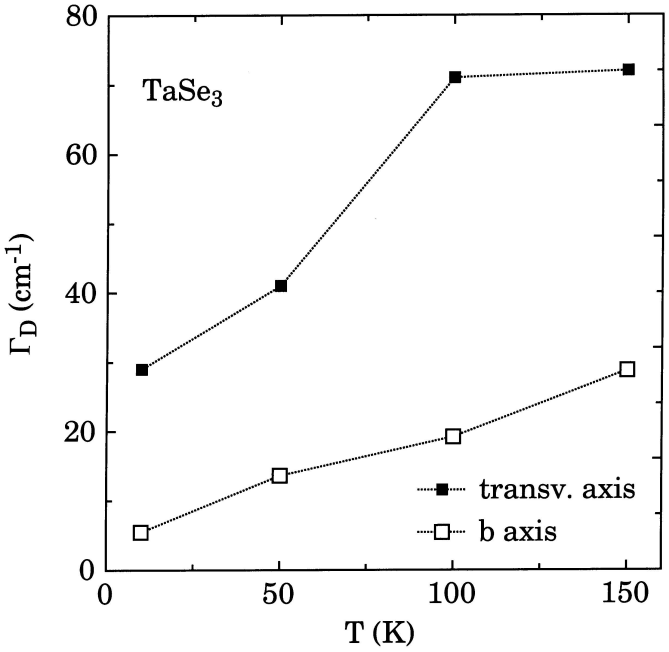

Fig. 9. Temperature dependence of the scattering rate for the Drude term in the LD fits to both polarization directions.

temperature. It can be stated that those MS's basically dissolve, merging into the Drude component and getting more mobile with decreasing temperature. Consequently, the MS's do not order in a long range ordered condensate and $TaSe_3$ fails to reach a CDW broken symmetry ground state. The broad mid-infrared feature in $\sigma_1(\omega)$ along the b-axis is then associated with the binding energy related to the formation of the MS's.

We now briefly comment on the temperature dependent narrowing of the Drude term for both polarization directions. This is represented by the decrease of the Drude scattering rate Γ_D, as shown in Figure 9. The suppression of scattering rate along the transverse axis is rather strong below 100 K and more gradual along the b-axis. This is pretty much in agreement with the overall behaviour of the dc-transport data (Fig. 1) and signals the freezing of scattering channels with decreasing temperature. The reduced scattering rate at low temperatures (i.e., $T < T_0$) is also consistent with the scenario postulating the disappearance of MS's (i.e., acting above T_0 as pinning and scattering centers) with decreasing temperature. For comparison, we mention that a pronounced decrease of the scattering rate was also encountered in $NbSe_3$ below the lowest CDW transition temperature of 59 K. This was ascribed to the formation of a CDW long range ordered condensate [7]. Therefore, either the dissolution of MS's or the condensation of CDW segments into a collective state lead to the freezing of scattering channels at low temperatures.

From the ARPES viewpoint, the unusual flat portion of the band observed just below E_F around Γ (Fig. 6), almost certainly plays an important role in determining the electronic properties of $TaSe_3$. It is therefore important to consider the implications of this observation, even if its origin cannot be conclusively determined from the spectroscopic data. We consider below three alternative scenarios.

The flat band could be a pure band-structure effect, due to hybridization with a symmetrically dispersing – i.e. mostly or totally unoccupied – band. The existing band structure calculations are of limited help, since they do not properly describe the energy position of the parabolic band. At least two unoccupied bands, with Ta d_{z^2} character, disperse upwards from minima at Γ in proximity of E_F (Ref. [15]), and the energy separation between the top of the "hole-like" and the bottom of one of the "electron-like" bands could be smaller than in the calculation. Hybridization would then yield a delimited region in k-space with a high density of states (DOS), favoring the development of a CDW instability, in the spirit of the "saddle-point" picture of reference [24]. The CDW wavevector would span the small flat-band region, so that the corresponding diffraction satellites would be quite close to Bragg peaks, and difficult to resolve. The resulting gap energy, estimated from the ARPES spectra to be ∼0.1 eV, coincides with the peak in the transverse optical conductivity. A difficulty with this scenario is the metallic dc resistivity (Fig. 1) and the finite ARPES intensity at E_F.

Alternatively, we could assume that the ARPES spectra reflect an underlying instability, and interpret the peak energy as the half-width of an associated pseudogap. This would be consistent with the ∼0.1 eV energy scale from optics, but also with the metallic character in the fluctuation regime [25,26]. We would however expect a reduction of the spectral intensity at E_F with decreasing temperature, following the opening of a real gap, which is not experimentally observed. Consistency with the data then requires some other mechanism (e.g., disorder) opposing the development of long-range coherence and hence the opening of a real gap.

Perhaps more convincing is the assumption that the ARPES data reflect strongly interacting carriers. In 1D Peierls (CDW) systems, like $K_{0.3}MoO_3$ or $(TaSe_4)_2I$ where the e-ph coupling is strong and poorly screened, the quasiparticles can be quite different from bare electrons. They are better described as polarons, i.e. electrons which move coherently with a local lattice deformation, and may eventually crystallize into an ordered CDW state [27]. The coherent QP weight is reduced and the effective mass enhanced, and most of the spectral weight may be transferred into an incoherent "polaronic" sideband shifted below the QP by the polaron binding energy. The main dispersing ARPES feature then does not correspond to the position of the QP, but rather to that of the incoherent sideband [28]. This mechanism, which stresses electron-phonon interactions, is distinct from the reduction of spectral weight at the Fermi surface predicted by the purely electronic Luttinger scenario. We make the hypothesis that hybridization produces flat bands around Γ, which pin the Fermi level. The associated coherent QP weight determines the finite spectral intensity at E_F, while the strong peak at 60 meV is associated with the polaronic

sideband. Notice that the sizable intensity at E_F and the "polaronic" energy shift are indicative of strong e-ph coupling, but not as strong as in $K_{0.3}MoO_3$ or $(TaSe_4)_2I$, where the coherent QP weight is almost entirely suppressed. This more elaborate scenario is consistent with all experimental results: i) the metallic conduction is explained, because the QPs are actually at E_F, even if their spectral signature is dominated by the polaronic sideband; ii) the 0.1 eV feature in the optical conductivity is also compatible with polaronic QPs; a simple but rather general approach [29] in fact predicts that $\sigma(\omega)$ should exhibit both a Drude peak – corresponding to the ARPES coherent QP weight – and a distinct feature at an energy equal to twice the polaron's binding energy, for sufficiently strong coupling.

4 Conclusion

The optical properties of $TaSe_3$, while anisotropic, do not display the signatures for a CDW phase transition, which would result from a FS gapping. The electrodynamic response as well as the dc transport properties suggest the presence of fluctuating short range order CDW segments, which apparently do not condense in a collective state. Strong interactions and the proximity to an instability are suggested by a high density of states near the Fermi level, and by peculiar ARPES line shapes. Comparing $TaSe_3$ with $NbSe_3$, we have demonstrated the relevance of the FS topology and, in particular, the importance of favorable nesting conditions, as necessary ingredient for the driving mechanism leading to the onset of broken symmetry ground states.

The authors wish to thank J. Müller and the SRC staff for technical help, and G. Caimi for fruitful discussions. This work has been supported by the Swiss National Foundation for the Scientific Research through the MaNEP NCCR. The Synchrotron Radiation Center, University of Wisconsin-Madison, is supported by NSF under Award No. DMR-0084402.

References

1. For a review see, *Strong Interactions in Low Dimensions*, edited by D. Baeriswyl, L. Degiorgi (Kluwer, 2003), and references therein
2. G. Grüner, in *Density waves in solids* (Addison Wesley, 1994), and references therein
3. V. Vescoli, F. Zwick, W. Henderson, L. Degiorgi, M. Grioni, G. Grüner, L.K. Montgomery, Eur. Phys. J. B **13**, 503 (2000)
4. V.J. Emery, S.A. Kivelson, Phys. Rev. Lett. **74**, 3253 (1995)
5. S.V. Dordevic, D.N. Basov, R.C. Dynes, B. Ruzicka, V. Vescoli, L. Degiorgi, H. Berger, R. Gaál, L. Forró, E. Bucher, Eur. Phys. J. B **33**, 15 (2003)
6. N.P. Ong, P. Monceau, Phys. Rev. B **16**, 3443 (1977)
7. A. Perucchi, L. Degiorgi, R.E. Thorne, Phys. Rev. B **69**, 195114 (2004)
8. J. Schäfer, Eli Rotenberg, S.D. Kevan, P. Blaha, R. Claessen, R.E. Thorne, Phys. Rev. Lett. **87**, 196403 (2001); J. Schäfer, M. Sing, R. Claessen, Eli Rotenberg, X.J. Zhou, R.E. Thorne, S.D. Kevan, Phys. Rev. Lett. **91**, 066401 (2003)
9. M. Núñez-Regueiro, Solid State Commun. **60**, 797 (1986)
10. E.N. Dolgov, Yu.I. Latyshev, V.E. Minakova, Sov. Phys. Solid State **26**, 2089 (1984)
11. B. Ruzicka, L. Degiorgi, H. Berger, R. Gaál, L. Forró, Phys. Rev. Lett. **86**, 4136 (2001)
12. N.E. Hussey, M. Kibune, H. Nakagawa, N. Miura, Y. Iye, H. Takagi, S. Adachi, K. Tanabe, Phys. Rev. Lett. **80**, 2909 (1998)
13. J. Moser, M. Gabay, P. Auban-Senzier, D. Jérome, K. Bechgaard, J. M. Fabre, Eur. Phys. J. B **1**, 39 (1998)
14. F. Wooten, in *Optical Properties of Solids* (Academic Press, New York, 1972); M. Dressel, G. Grüner, in *Electrodynamics of Solids* (Cambridge University Press, 2002)
15. E. Canadell, I.E.-I. Rachidi, J.P. Pouget, P. Gressier, A. Meerschaut, J. Rouxel, D. Jung, M. Evain, M.-H. Whangbo, Inorg. Chem. **29**, 1401 (1990)
16. C.G. Slough, B. Giambattista, W.W. McNairy, R.V. Coleman, J. Vac. Sci. Technol. A **8**, 490 (1990)
17. S. Hüfner, *Photoelectron Spectroscopy* (Springer Verlag, Berlin, 1995)
18. D.W. Bullett, J. Phys. C **12**, 277 (1979)
19. A. Schwartz, M. Dressel, B. Alavi, A. Blank, S. Dubois, G. Grüner, B.P. Gorshunov, A.A. Volkov, G.V. Kozlov, S. Thieme, L. Degiorgi, F. Lévi, Phys. Rev. B **52**, 5643 (1995)
20. C.C. Yu, P.W. Anderson, Phys. Rev. B **29**, 6165 (1984)
21. T.M. Tritt, in *Proceedings of 17th Int. Conf. on Low Temperature Physics*, edited by U. Eckern, A. Schmidt, W. Weber, H. Wuehl (Noth Holland Amsterdam, 1984), p. 1334
22. T. Valla, P.D. Johnson, Z. Yusof, B. Wells, Q. Li, S.M. Loureiro, R.J. Cava, M. Mikami, Y. Mori, M. Yoshimura, T. Sasaki, Nature **417**, 627 (2002)
23. D.N. Basov, S.I. Woods, A.S. Katz, E.J. Singley, R.C. Dynes, M. Xu, D.G. Hinks, C.C. Homes, M. Strongin, Science **283**, 49 (1999) and references therein
24. T.M. Rice, G.K. Scott, Phys. Rev. Lett. **35**, 120 (1975)
25. P.A. Lee, T.M. Rice, P.W. Anderson, Solid State Commun. **14**, 703 (1974)
26. N. Shannon, R. Joynt, J. Phys.: Condens. Matter **8**, 10493 (1996)
27. J.-L. Raimbault, S. Aubry, J. Phys.: Condens. Matter **7**, 8287 (1995)
28. L. Perfetti, H. Berger, A. Reginelli, L. Degiorgi, H. Höchst, J. Voit, G. Margaritondo, M. Grioni, Phys. Rev. Lett. **87**, 216404 (2001)
29. D. Emin, Phys. Rev. B **48**, 13691 (1993)